

# Modelling and measuring the thermal behaviour of the molten pool in closed-loop controlled laser-based additive manufacturing

D Hu and R Kovacevic\*

Research Center for Advanced Manufacturing, Southern Methodist University, Richardson, Texas, USA

**Abstract:** Laser-based additive manufacturing (LBAM) is a promising manufacturing technology that can be widely applied in solid freeform fabrication (SFF), component recovery and regeneration, and surface modification. The thermal behaviour of the molten pool is one of the critical factors that influences laser deposition indices such as geometrical accuracy, material properties and residual stresses. In this paper, a three-dimensional finite element model is developed using ANSYS to simulate the thermal behaviour of the molten pool in building a single-bead wall via a closed-loop controlled LBAM process in which the laser power is controlled to keep the width of the molten pool constant. The temperature distribution, the geometrical feature of the molten pool and the cooling rate under different process conditions are investigated. To verify the simulation results, the thermal behaviour of the molten pool is measured by a coaxially installed infrared camera in experimental investigations of a closed-loop controlled LBAM process. Results from finite element thermal analysis provide guidance for the process parameter selection in LBAM, and develop a base for further residual stress analysis.

**Keywords:** solid freeform fabrication, laser deposition, finite element modelling

## NOTATION

$A$	absorption rate of laser power on the metal surface	$r$	distance from the centre of the laser beam (m)
$C, c$	specific heat (J/kg K)	$r_b$	effective laser beam radius (m)
$C_1$	first radiation constant ( $1.191062 \times 10^8 \text{ W } \mu\text{m}^4 \text{ m}^2 \text{ sr}$ )	$t$	time (s)
$C_2$	second radiation constant ( $1.438786 \times 10^4 \mu\text{m K}$ )	$T$	temperature (K)
$E_\lambda, E$	spectral radiance ( $\text{W/m}^2 \text{ sr}$ )	$T_{\text{mes}}$	measured spectral radiance temperature of the target (K)
$h$	heat transfer coefficient ( $\text{W/m}^2 \text{ K}$ ), height of the wall (m)	$T_{\text{true}}$	true temperature of the measured target (K)
$H$	enthalpy (J/kg)	$T_0$	ambient temperature (K)
$I$	thermal flux density of the laser beam ( $\text{J/s m}^2$ )	$v$	traverse velocity (m/s)
$k$	thermal conductivity ( $\text{J/m s K}$ )	$w$	width of the wall (m)
$k_n$	thermal conductivity normal to $S_2$ ( $\text{J/m s K}$ )	$x, y, z$	coordinate system (m)
$L$	length of the wall (m)	$\varepsilon$	surface emissivity
$P$	laser power (J/s)	$\varepsilon_\lambda$	spectral emissivity
$q$	heat flux normal to $S_2$ ( $\text{W/m}^2$ )	$\lambda$	wavelength ( $\mu\text{m}$ )
$Q$	power generation per unit volume ( $\text{W/m}^3$ )	$\rho$	density ( $\text{kg/m}^3$ )
		$\sigma$	Stefan–Boltzmann constant for radiation ( $5.67 \times 10^{-8} \text{ W/m}^2 \text{ K}^4$ )

## 1 INTRODUCTION

Laser-based additive manufacturing (LBAM) is a promising manufacturing technology that can be widely applied to component recovery and regeneration, surface

The MS was received on 16 July 2002 and was accepted after revision for publication on 29 November 2002.

\*Corresponding author: RCAM, Southern Methodist University, 1500 International Parkway, Suite 100, Richardson, TX 75081, USA.

modification and solid freeform fabrication (SFF). It brings great advantages such as reducing the lead time from design to part production, material tailoring and microstructure control. The thermal behaviour of the molten pool is critical to the results of the LBAM process. The bead width, which decides the geometrical accuracy of deposition, is identical to the width of the molten pool. The cooling rate at the liquid–solid transient boundary of the molten pool determines the solidification process and microstructure. The temperature distribution decides the thermal residual stresses. A large number of parameters govern the LBAM process, such as the absorption of laser power, powder delivery rate, powder deposition efficiency, traverse velocity, etc. These parameters are sensitive to environmental variations and ultimately influence the thermal behaviour of the molten pool. In order to obtain a robust and controllable laser deposition process, modelling and sensing of LBAM are required to understand the thermal behaviour of the molten pool.

Single-bead wall building provides a good opportunity for modelling and sensing the thermal behaviour of the molten pool in LBAM. It is a basic geometrical feature built by LBAM and experiences critical processing conditions. There have been numerous studies reported on numerical modelling and sensing of laser material processing, such as laser welding and laser cladding [1–8]. However, only a few of them have focused on

modelling and sensing of the building of a single-bead wall by the laser deposition process [9, 10], and the model is limited to two-dimensional analyses without considering the influence of the thickness of the wall. The difficulties of establishing a three-dimensional numerical model to simulate the process of building a single-bead wall lie in the variation in the molten pool. The thickness of the wall is identical to the width of the molten pool, which is determined by the processing parameters (laser power, traverse velocity, etc.) and heat balance conditions. The width of the molten pool varies in the open-loop LBAM process according to the processing conditions in a complex relationship. A three-dimensional numerical model with a constant wall thickness and a predefined laser input power is not sufficiently accurate to simulate LBAM processes under different processing conditions.

The complexity in numerical modelling that is caused by variation in the molten pool can be regulated by the closed-loop controlled LBAM process [11]. The single-bead wall building process based on closed-loop controlled LBAM is illustrated in Fig. 1. The continuous wave (CW) mode Nd:YAG (neodymium-doped yttrium aluminium garnet) laser is projected by the laser head onto the moving substrate (along the  $y$  direction) to create a molten pool. The metal powder is delivered into the molten pool through the coaxial nozzle and adheres to the substrate to create a single-bead layer.

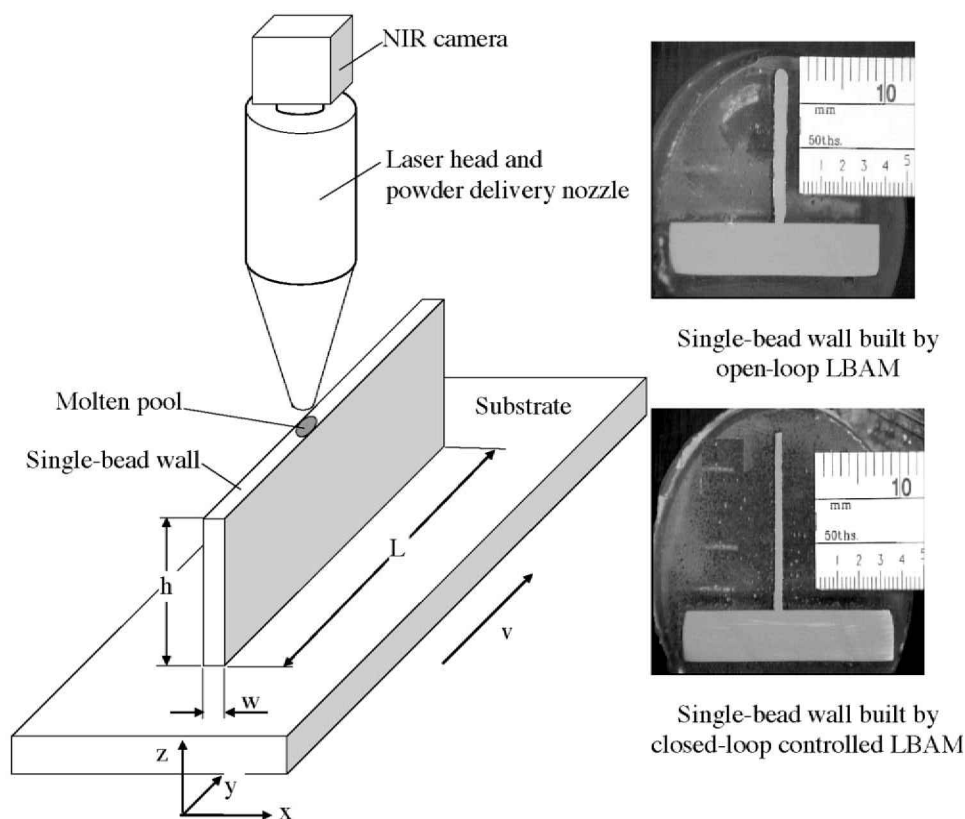


Fig. 1 Closed-loop controlled LBAM process

By increasing the nozzle position in the  $z$  direction after one layer is finished, next layers are built repeatedly on previous layers so that a single-bead wall can be generated. In closed-loop controlled LBAM, the geometrical feature of the molten pool is sensed by a near-infrared camera coaxially installed with the laser head. The width of the molten pool acquired from the infrared image is used as a feedback to control the laser output power. In such a way, a constant width of the molten pool can be achieved in the LBAM process, and a single-bead wall with a uniform thickness can be built. The intersections of the walls built by open-loop LBAM and closed-loop controlled LBAM are also shown in Fig. 1. Closed-loop controlled LBAM ensures a constant laser processing condition that results in a better performance for the geometrical accuracy, and brings regulation to the microstructure and residual stresses of the part. It also enables the establishment of a simpler but more realistic numerical model for single-bead wall building in which a constant wall thickness can be applied.

In this paper, a three-dimensional finite element model is developed using ANSYS to study the thermal behaviour of the molten pool in building a single-bead wall via a closed-loop controlled LBAM process. The building process of one layer on the top of the single-bead wall with a certain height  $h$  is simulated. The model of the single-bead wall has a constant thickness  $w$ . The input laser power is controlled to ensure that the width of the molten pool is identical to the thickness of the wall during the deposition process. The temperature distribution, the geometrical feature of the molten pool and the cooling rate for different process conditions are investigated. To verify the simulation results, the thermal behaviour of the molten pool is measured by the coaxially installed infrared camera in experimental investigations of the closed-loop controlled LBAM process. Results from finite element thermal analysis provide guidance for the process parameter selection in LBAM, and develop a base for further residual stress analysis.

## 2 DESCRIPTION OF THE MODEL

Since LBAM is a thermal process, the well-known heat conduction equation plays a central role in the physical modelling of the process. The heat conduction equation follows from the energy balance of an appropriately chosen volume and consists of the diffusive heat flows, the convective heat flows and the possible sources of heat [12]. The thermal equilibrium equation for the analysis of the heat transfer in a domain  $D$  can be written as

$$k \left( \frac{\partial^2 T}{\partial x^2} + \frac{\partial^2 T}{\partial y^2} + \frac{\partial^2 T}{\partial z^2} \right) + q = \rho c \left( \frac{\partial T}{\partial t} \times v \frac{\partial T}{\partial y} \right) \quad (1)$$

To obtain the solution from the thermal equilibrium equation, the boundary conditions and the initial conditions are needed.

The initial conditions are

$$\begin{aligned} T(x, y, z, 0) &= T_0 & \text{for } (x, y, z) \in D \\ T(x, y, z, t) &= T(x, y, z, t \times \Delta t) & \text{for } (x, y, z) \in D \end{aligned} \quad (2)$$

The essential boundary condition is

$$T(x, y, z, t) = T_0 \quad (3)$$

on the boundary  $S_1$  for  $(x, y, z) \in S_1$  and  $t > 0$ ;  $S_1$  represents the bottom surface of the plate.

The natural boundary conditions can be defined by

$$k_n \frac{\partial T}{\partial n} \times q + h(T \times T_0) + \sigma \varepsilon (T^4 \times T_0^4) = 0 \quad (4)$$

on the boundary  $S_2$  for  $(x, y, z) \in S_2$  and  $t > 0$ ;  $S_2$  represents those surfaces that are subjected to radiation, convection and imposed heat fluxes.

The inclusion of the temperature dependent thermo-physical properties and a radiation term in the above boundary condition makes this type of analysis highly non-linear. Since the incorporation of radiation effects is found to increase the solution by as much as a factor of 3, an empirical relationship as proposed by Vinokurov [13] is used:

$$h = 2.4 \times 10^3 \varepsilon T^{1.61} \quad (5)$$

Equation (5) combines the effect of radiation and convection into a 'lumped' heat transfer coefficient. The associated loss in accuracy using this relationship is estimated to be less than 5 per cent [13].

From the above analysis of the physical phenomena, the following assumptions can be made:

1. The workpiece is initially at 298 K, which means there is enough waiting for the workpiece to cool down between the building of each layer. Both the workpiece and the coordinate mesh are fixed, and the laser beam moves in the positive  $y$  direction with a constant velocity,  $v$ .
2. All thermophysical properties are considered to be temperature dependent. These properties are given in Table 1 [14].
3. The laser beam diameter is defined as the diameter in which the power density is reduced from the peak value by a factor of  $e^2$  [15].
4. During the simulation, the thermal load is given in the form of the thermal flux density which obeys a normal distribution as follows [14]:

$$I = \frac{2AP}{\pi r_b^2} \exp \left( -\frac{2r^2}{r_b^2} \right) \quad (6)$$

**Table 1** Thermophysical properties used in the finite element model

Temperature (K)	Thermal conductivity (W/m K)	Specific heat (J/kg K)	Density (kg/m <sup>3</sup> )
273	51.9	450	7872
348	51.3	486	7852
373	51.1	494	7845
448	49.5	519	7824
573	49	526	7816
498	48.3	532	7809
548	46.8	557	7763
573	46.1	566	7740
598	45.3	574	7717
648	43.6	599	7727
673	42.7	615	7733
748	40.2	662	7720
773	39.4	684	7711
848	36.6	749	7680
873	35.6	773	7669
948	32.8	846	7636
973	31.8	1139	7625
1003	30.1	1384	7612
1023	28.9	1191	7602
1048	27.5	950	7590
1073	26	931	7578
1273	27.2	779	7552
1600	29.7	400	7268
1785	29.7	847	7055
2113	29.7	847	6757
2163	29.7	400	6715
3000	29.7	400	5902

The mean thermal flux density within the area of the laser beam scanning is [14]

$$I_m = \frac{1}{\pi r_b^2} \int_0^{r_b} I(2\pi r) dr$$

$$= \frac{2\pi}{\pi r_b^2} \int_0^{r_b} \frac{2AP}{\pi r_b^2} \exp\left(\times \frac{2r^2}{r_b^2}\right) r dr = \frac{0.865AP}{\pi r_b^2} \quad (7)$$

5. The latent heat of fusion is simulated by an artificial increase in the liquid specific heat according to Brown and Song [16] and the relationship between the enthalpy,  $H$ , density,  $\rho$  and specific heat,  $c$ :

$$H = \int \rho c(T) dT \quad (8)$$

An additional value can be added to the latent heat of the top layer to take into account the energy absorption by the metal powder particles. However, to simplify the problem, no material adding is considered in this study.

6. Since LBAM involves very rapid melting and solidification, the convective redistribution of heat within the molten pool is not significant. The convective flow of heat, therefore, is neglected.

ANSYS provides convenient means of numerically modelling the LBAM process. In this simulation, transient analysis is performed to fit the requirements of the process. In finite element analysis formulation, the

equation can be written for each element as

$$[C(T)]\{\dot{T}\} + [K(T)]\{T\} = \{Q(T)\} \quad (9)$$

The meshed finite element model of the single-bead wall with a height  $h$  and thickness  $w$  is shown in Fig. 2. The model is meshed with an eight-node brick element. The size of the elements in the top layer is controlled, so a fine mesh can be achieved in the layer concerned, and the further heat flux boundary condition can be applied on the nodes with accurate position. A free mesh is carried onto the remainder of the wall and the substrate, and the eight-node brick element degrades to a tetrahedral element. The moving laser beam will be simulated automatically using an ANSYS parametric design language (APDL) program to provide a heat flux boundary condition (absorbed laser energy) at different positions, times and values. Iteration is introduced into the program to find the proper value of the heat flux that results in an identical width of the molten pool to the wall thickness of the model. The solving algorithm is presented in Fig. 3.

### 3 MEASURING THE THERMAL BEHAVIOUR OF THE MOLTEN POOL

A coaxially installed image-sensing set-up with respect to the laser head and powder delivery nozzle is applied in the LBAM system to measure the thermal behaviour of the molten pool and to provide the feedback for closed-loop control. As shown in Fig. 4, a high frame rate  $128 \times 128$  CCD (charge-coupled device) camera is installed on top of the laser head to acquire the infrared image of the molten pool through the same optical path for the Nd:YAG laser focusing. In order to obtain an infrared image of the molten pool that reduces the high-intensity light from the molten pool and eliminates the image noise from the metal powder, a near-infrared filter is selected ( $>700\text{nm}$ ) and installed between the iris and the camera. An Nd:YAG laser blocker ( $1.06\mu\text{m}$ ) is utilized to protect the camera from laser damage. The wavelength band of radiation received by the camera is  $0.7\text{--}1.06\mu\text{m}$ , which is an efficient spectral band to measure the temperature of incandescent metals in the range of  $700\text{--}3200\text{K}$  [17]. A full-view, clear infrared image of the molten pool can be acquired by such a set-up (Fig. 4), and it is omnidirectional to the traverse directions. During the laser deposition process, the camera acquires images of the molten pool at a frame rate of 300 frames/s. Images are transferred to the frame grabber installed on a PC. The computer carries out further image processing and the control process.

The infrared camera is calibrated first with a black body to find the response of the camera to the measured temperature. To eliminate the error caused by the different transmission paths of radiation [18], the black

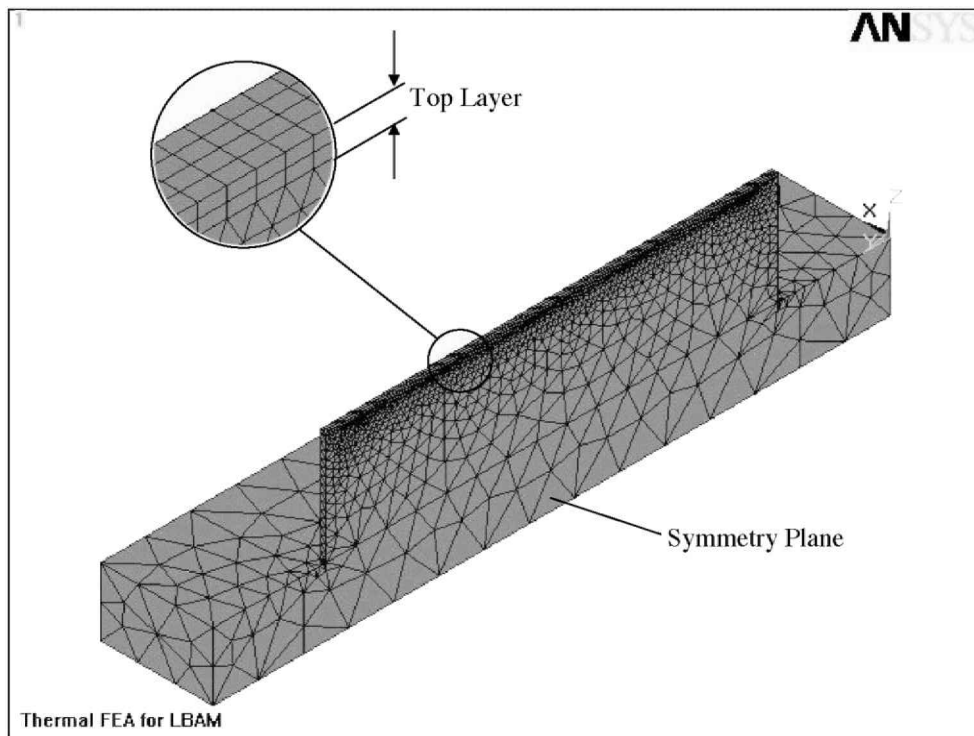


Fig. 2 Finite element mesh model

body is placed right under the nozzle with the same distance as the nozzle–substrate distance for the laser deposition. The NIR image of the heated black body is recorded at 300 frames/s simultaneously with the temperature measured by a B-type thermocouple. The

relationship between the grey level of the NIR image pixel and the black body temperature is given in Fig. 5 by the curve with an emissivity of 1.0.

According to Planck's law, the spherical or total radiance is linked to the temperature of a black body

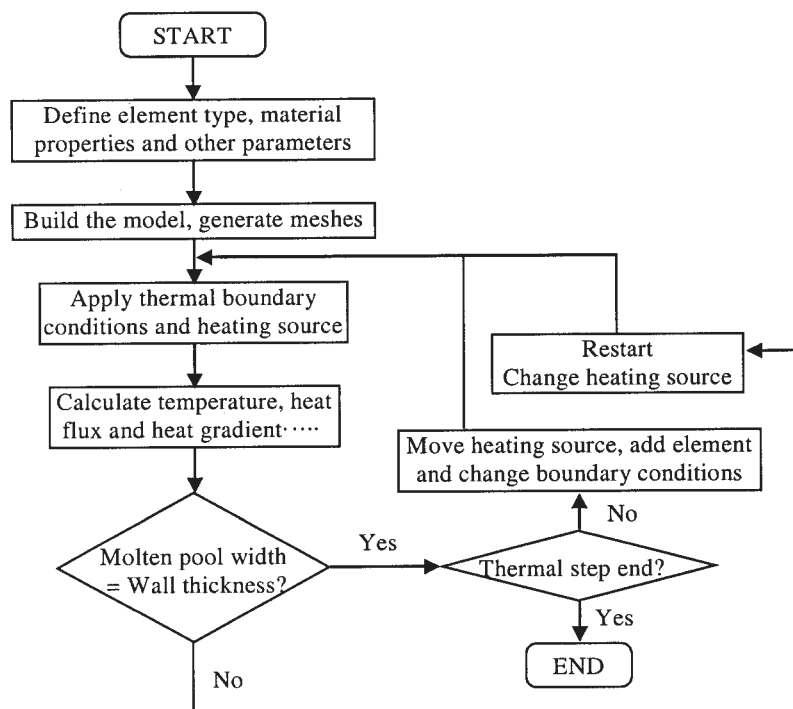


Fig. 3 Simulation algorithm

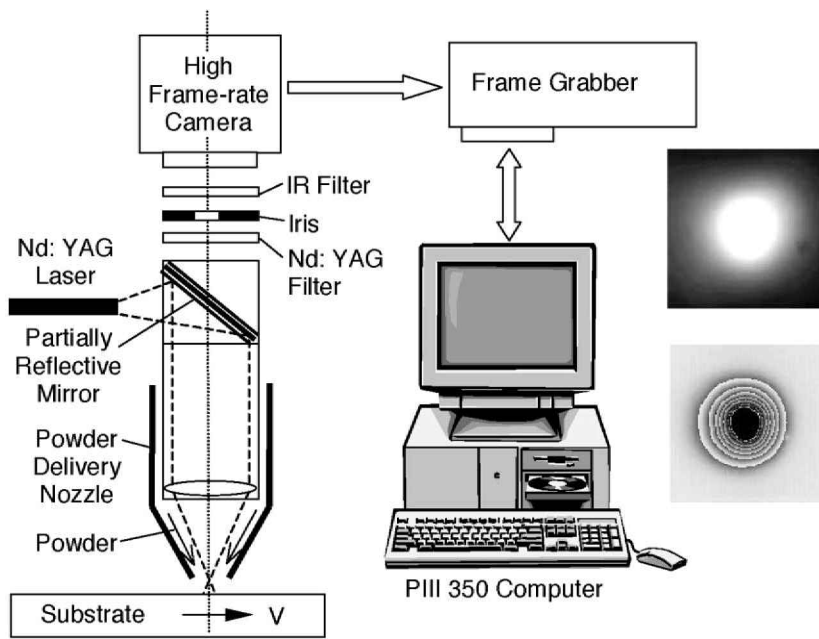


Fig. 4 Infrared image acquisition system

by the equation

$$E(T, \lambda) = \frac{C_1 / \lambda^5}{\exp(C_2 / \lambda T) \times 1} \quad (10)$$

where  $C_1$  and  $C_2$  are Planck's constants.

Using Planck's law, the true temperature can be inferred from the measured temperature through the relation

$$E_\lambda(T_{\text{mes}}) = \varepsilon_\lambda L_\lambda(T_{\text{true}}) \quad (11)$$

where  $\varepsilon_\lambda$  is the target emissivity.

Taking the familiar form

$$\frac{1}{T_{\text{true}}} = \frac{1}{T_{\text{mes}}} + \frac{\lambda}{C_2} \ln \varepsilon_\lambda \quad (12)$$

derived from Wien's law (an approximation of Planck's law for  $C_2 \gg \lambda T$ ) for the black-body spectral radiance,

the temperature of the target with different emissivities can be calculated (Fig. 5). The emissivity of molten steel is 0.3. It can be seen in Fig. 5 that the pixel grey value corresponding to the melting point of mild steel (1785 K) is 70. The temperature that the camera can measure is 1600–2100 K for such emissivity. In laser deposition, an emissivity lower than 0.3 is expected owing to the existence of metal powder.

The edge of the molten pool provides the geometrical feature of the bead. The end edge of the molten pool is also the area of concern where the solidification occurs and the cooling rate must be controlled to achieve the desired microstructure. To verify the position of the edge of the molten pool from the NIR image, an additional high shutter speed camera is installed beside the laser head, with a fibre-optic cable that conducts a 337 nm near-UV laser to illuminate the molten pool and its surrounding area. The camera includes an

### NIR Image Calibration (300 Frames/S)

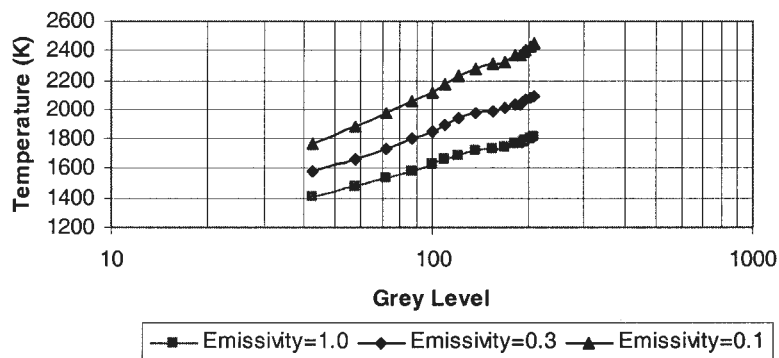


Fig. 5 Relationship between grey level and temperature for different emissivities

ultraviolet filter that only allows light with a wavelength near 337 nm to pass. The illuminating laser is a pulsed laser with a 5 ns pulse duration synchronized with the shutter of the camera. The camera shutter opens for 50 ns to capture one image as the illuminating laser is triggered. During the illumination period, the intensity of the illuminating laser can overpower the spatter and plasma light. Owing to the reflection of the mirror-like molten pool, a well-contrasted image of the molten pool can be obtained.

Images of the molten pool are acquired simultaneously by the two cameras during laser processing. In order to acquire a clear image from the high shutter speed camera, no metal powder is delivered. The images acquired by the two cameras are shown in Figs 6a and b. Both cameras are calibrated first by a grid-patterned target. The unit on the cross-lines in Fig. 6 is 0.1 mm. A modified Canny-edge detector is applied to the normal image acquired by the high shutter speed camera to detect the edge of the molten pool [19]. The edge of the molten pool in the NIR image is determined by the isotherm of the melting point temperature of the

mild steel substrate. The edges extracted from the two images are not exactly identical to each other for two reasons. The high shutter speed camera is operated at a 30 Hz frame rate, so there is a maximum 30 ms time interval between the acquisition of the NIR image and the grey level image. Secondly, the vapour and hot air above the molten pool may slightly distort the NIR image. However, there is a good match on the width, length and area of the molten pool measured from both the images. Such a match verifies that the NIR image can accurately measure the temperature and geometrical features of the molten pool.

#### 4 DISCUSSIONS ON MODELLING AND MEASUREMENT RESULTS

A numerical simulation is carried out to analyse the thermal behaviour of the molten pool in the closed-loop controlled LBAM process. Figure 7 shows the results of simulation of one-layer building applying the following process parameters:  $v = 5$  mm/s,  $w = 1$  mm,  $h = 10$  mm and  $L = 40$  mm. The laser power parameter in Fig. 7 is proportional to the laser output power and is adjusted according to the shape of the molten pool. By varying the laser power, the maximum temperature on the wall edge is controlled around the melting point, so the width of the molten pool is identical to the width of the wall. In the simulation, the maximum temperature on the wall edge is controlled in the range 1785–1788 K. The shape of the molten pool and the fusion depth are constant during the layer building in spite of the variations in the cooling conditions. In the simulation of building one layer, the cooling condition changes at the two ends of the wall. During the wall building process, the cooling condition varies with the height of the wall, substrate temperature, etc.

The molten pool is also measured by the infrared imaging system to verify the simulation results. Closed-loop controlled LBAM experiments are carried out so the infrared images of the molten pool in the processes can be acquired. As shown in Fig. 8a, the width of the molten pool is consistent in the process owing to the efforts of the closed-loop control. There are minor differences in the shape of the molten pool between the simulation result and measurement result. The shape differences are caused by the assumptions in the simulation that the convection inside the molten pool is ignored, and the wall edge keeps its geometrical shape even when it reaches the melting temperature. However, the simulation results agree well with experimental results in geometrical features such as the width and length of the molten pool. The experimental result shows that the numerical model achieves sufficient accuracy to simulate the closed-loop controlled LBAM process.

The average temperature in the laser–material interaction zone dominates the thermal residual stresses.

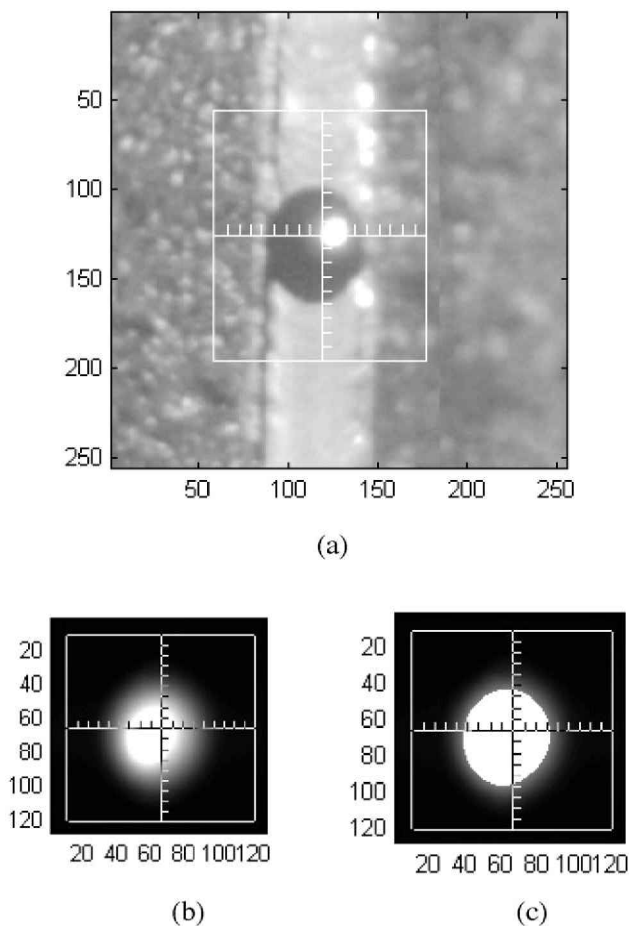


**Fig. 6** Images of molten pool: (a) ordinary image acquired by high shutter speed camera; (b) NIR image acquired by high frame rate camera; (c) isotherm of melting point temperature

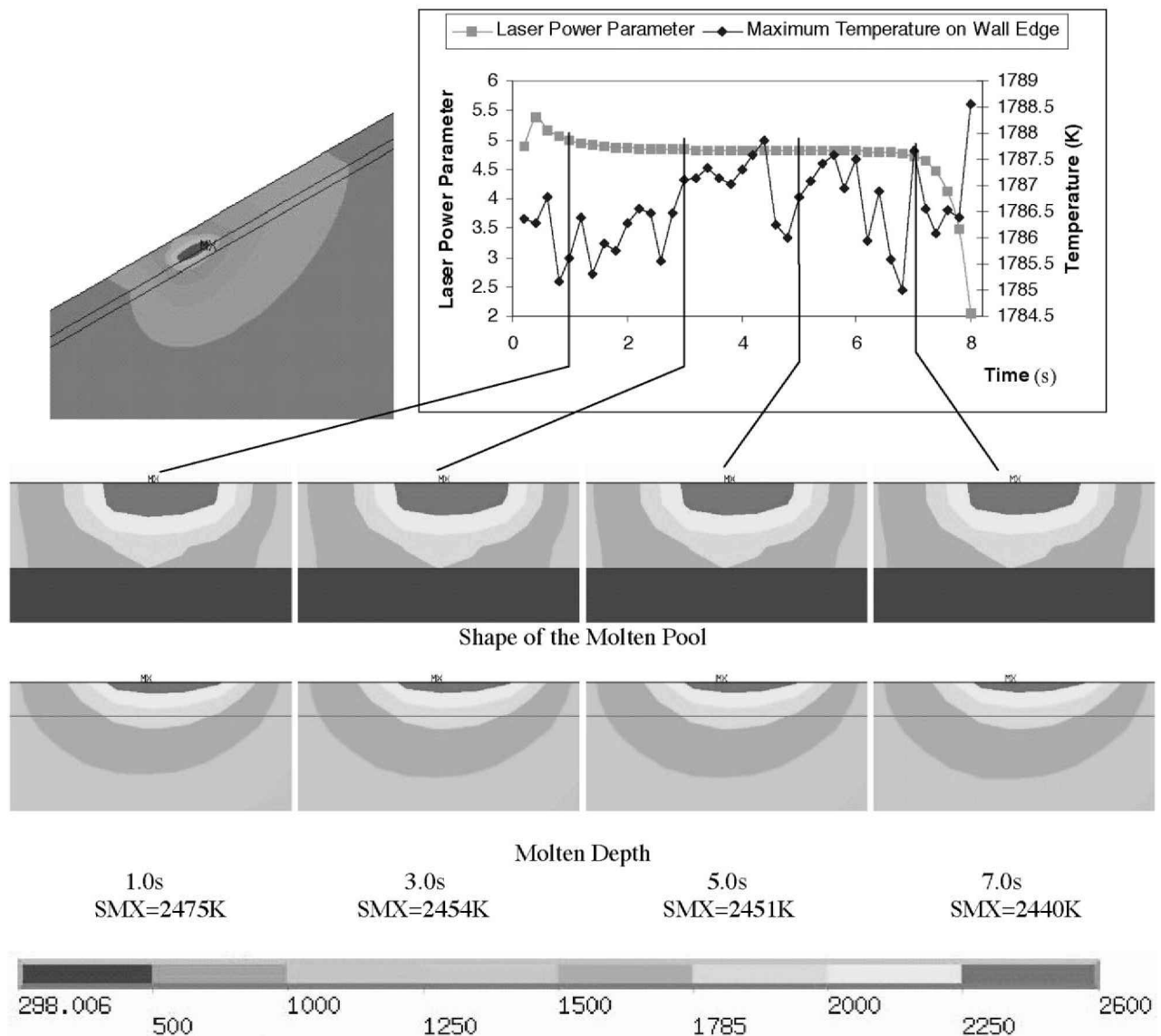


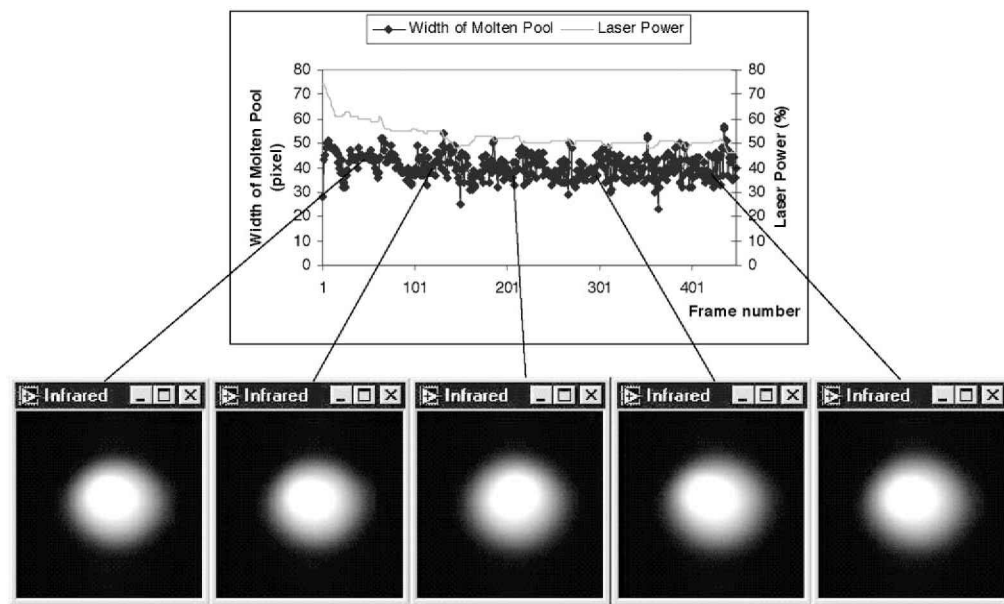
Fig. 7 Simulation results of one-layer building by closed-loop controlled LBAM

The cooling rate of solidification at the edge of the molten pool determines the microstructure. The fusion depth decides the combinations of the two layers and influences the quality of the previous layer. This thermal behaviour of the molten pool is not easily measured by the infrared camera but can be analysed from the numerical simulation results. Figure 9 gives the average temperature in the processing zone and the average cooling rate on the edge of the molten pool from the same simulation result shown in Fig. 7. Although the average cooling rate on the edge of the molten pool is much less than the cooling rate of solidification owing to the 0.2 s time interval in the simulation, it reflects the qualitative trends of the cooling rate of solidification. The corresponding results from simulation of uncontrolled LBAM are also provided for comparison. The curves in Fig. 9 show that controlled LBAM achieves a more stable average temperature that predicts even thermal

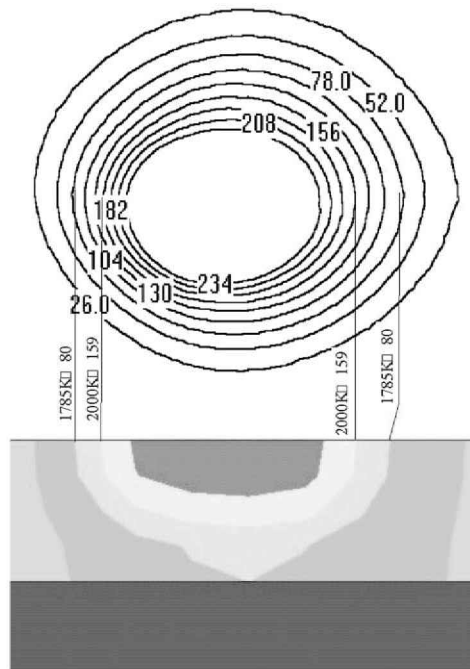
residual stresses. The cooling rate is heavily influenced by the cooling conditions (in this case, the heat conduction in different positions). However, it can be regulated in a smaller range by controlling the heat input. Such improvement results in more uniform microstructures.

Different combinations of traverse velocity and width of the wall are applied in different simulations to investigate the influences brought by the processing parameters. Figure 10 provides the simulation and experimental results. The length of the molten pool is measured from the infrared image, and the molten depth is measured from the cross-section of the sample. The simulation results match the experimental results within an acceptable tolerance. The maximum difference between the simulation results and the experimental results reaches 10 per cent for the molten depth and 4.5 per cent for the length of the molten pool when the target value of





(a)



(b)

**Fig. 8** Measurement results of one-layer building by closed-loop controlled LBAM: (a) control and feedback signals acquired in closed-loop controlled LBAM; (b) comparison of measurement and simulation results

the wall thickness is set to 1.5 mm. Such differences result from simplification of the model of complicated laser processing. Verified by the experimental results, the simulation results reveal the trends of influences of the processing parameters. It can be seen from Fig. 10

that, as the target width of the molten pool increases, the depth and length of the molten pool and the average temperature in the processing zone increase as well. For the process in which the width of the molten pool is kept constant, the traverse velocity contributes little to the

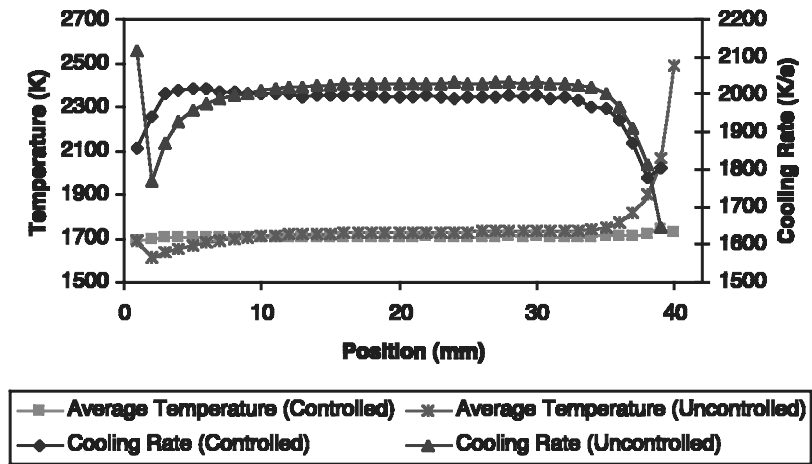


Fig. 9 Simulation results of average temperature and cooling rate

variations in the geometrical features of the molten pool. Although, as the traverse velocity increases, the average temperature in the processing zone decreases, the changes in the average temperature are prominent only when the traverse velocity is low and the wall thickness is small. The average cooling rate is influenced significantly by the traverse velocity. A roughly proportional relationship can be found between the traverse velocity and the average cooling rate. Although the average cooling rate decreases as the width of the molten pool

increases, the variation is only considerable when the traverse velocity is high. It can be concluded that the fusion depth and the average temperature in the processing zone can be regulated effectively by controlling the width of the molten pool at a constant traverse velocity; by contrast, the desired average cooling rate can be reached by changing the traverse velocity. Whenever a constant width of the molten pool is achieved, constant geometrical features of the molten pool are obtained. Therefore, controlling the area of the molten pool

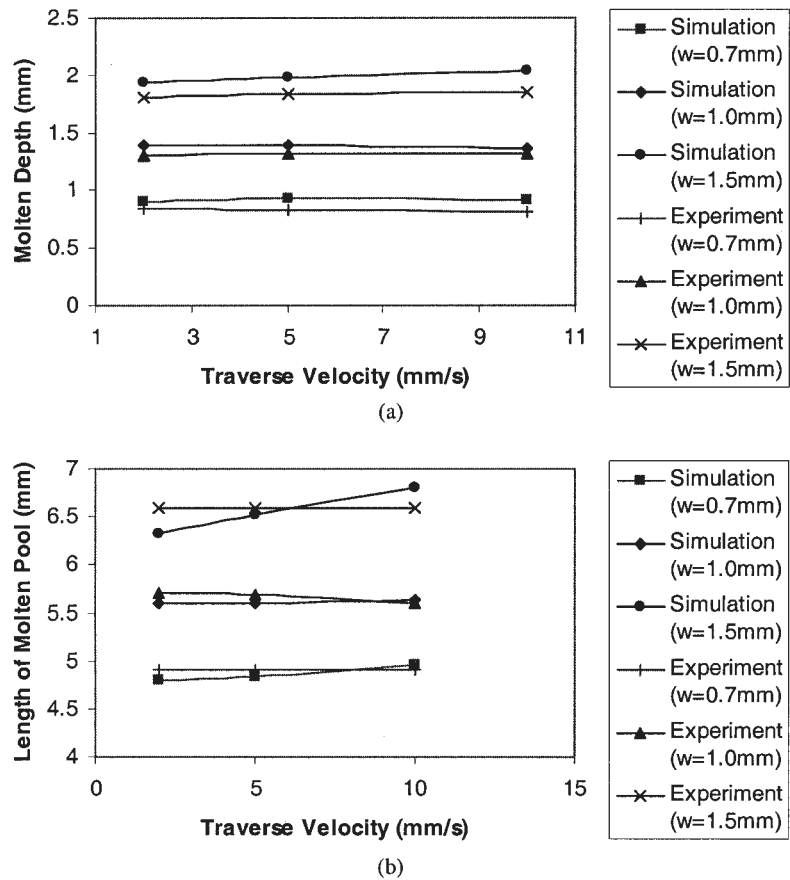


Fig. 10 (continued over)

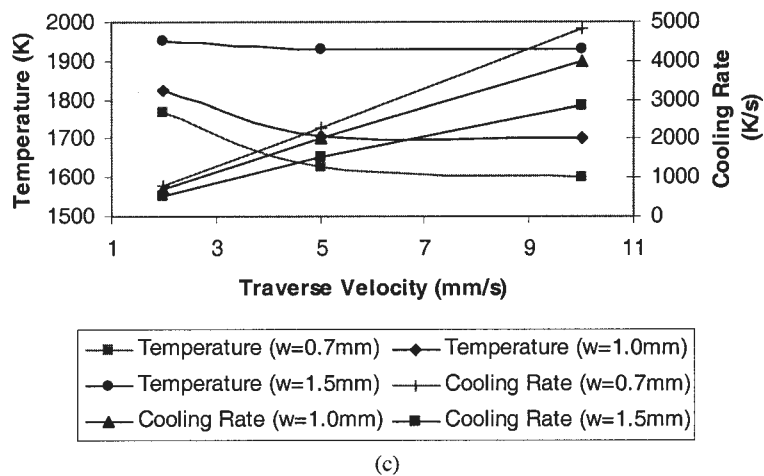


Fig. 10 Simulation results for different processing conditions: (a) depth of the molten pool; (b) length of the molten pool; (c) average temperature and cooling rate

involves the same effort as controlling the width of the molten pool.

## 5 CONCLUSIONS

A three-dimensional finite element model is developed successfully using ANSYS to study the thermal behaviour of the molten pool in building a single-bead wall via a closed-loop controlled LBAM process. The wall building process is also measured by an infrared imaging system. The simulation results agree with experimental results within an acceptable tolerance and reveal the trends of influences of the processing parameters. The simulation and experimental results show that the fusion depth and the average temperature in the processing zone can be regulated effectively by controlling the width or area of the molten pool at a constant traverse velocity. In closed-loop controlled LBAM, the influence of traverse velocity on the geometrical features of the molten pool can be ignored. Moreover, the effect of traverse velocity on the average temperature in the processing zone is limited, especially when the traverse velocity is in the high-speed range. Different desired average cooling rates can be achieved by applying different traverse velocities. A better performance with respect to geometrical accuracy and regulation of the microstructure and residual stresses is expected in the closed-loop controlled LBAM process.

## ACKNOWLEDGEMENTS

This work was financially supported by the Texas Higher Education Coordinating Board (THECB), Grant 003613-0022-1999, the National Science Foundation, Grants DM1-9732848 and DM1-9809198, and the US Department of Education, Grant P200A80806-98. Assistance by Mr M. Valant, research engineer, during experiments is gratefully acknowledged.

## REFERENCES

- 1 Mackerle, J. Finite element analysis and simulation of welding: a bibliography (1976–1996). *Modelling and Simulation in Mater. Sci. Engng*, 1996, **4**(5), 501–524.
- 2 Shiomi, M., Yoshidome, A., Abe, F. and Osakada, K. Finite element analysis of melting and solidifying processes in laser rapid prototyping of metallic powders. *Int. J. Mach. Tools Mf.*, 1999, **39**, 237–252.
- 3 Kim, J. and Peng, Y. Melt pool shape and dilution of laser cladding with wire feeding. *J. Mater. Processing Technol.*, 2000, **104**(3), 284–293.
- 4 Picasso, M. and Hoadley, A. F. A. Finite element simulation of laser surface treatments including convection in the melt pool. *Int. J. Numer. Meth. for Heat and Fluid Flow*, 1994, **4**(1), 61–83.
- 5 Carmignani, C., Mares, R. and Toselli, G. Transient finite element analysis of deep penetration laser welding process in a singlepass butt-welded thick steel plate. *Computer Meth. Appl. Mechanics Engng*, 1999, **179**(3), 197–214.
- 6 Hirsch, J. W., Olson, L. G., Nazir, Z. and Alexander, D. R. Axisymmetric laser welding of ceramics: comparison of experimental and finite element results. *Optics and Lasers in Engng*, 1998, **29**(6), 465–484.
- 7 Yang, Y. S. and Na, S. J. Study on the thermal and residual stress by welding and laser surface hardening using a new two-dimensional finite element model. *Proc. Instn Mech. Engrs, Part B: J. Engineering Manufacture*, 1990, **204**(3), 167–173.
- 8 Weerasinghe, V. M. and Steen, W. M. Computer simulation model for laser cladding. In *Transport Phenomena in Material Processing* (Eds M. M. Chen *et al.*), 1983, pp. 15–23 (American Society of Mechanical Engineers, New York).
- 9 Vasinonta, A., Beuth, J. L. and Griffith, M. A process map for consistent build conditions in the solid freeform fabrication of thin-walled structures. *J. Mfg Sci. Engng*, November 2002, **123**, 615–622.
- 10 Griffith, M. L., Schlienger, M. E., *et al.* Understanding thermal behaviour in the LENS process. *J. Mater. Des.*, 1999, **20**(2/3), 107–114.

- 11 **Hu, D., Mei, H. and Kovacevic, R.** Improving solid freeform fabrication by laser based additive manufacturing. *Proc. Instn Mech. Engrs, Part B: J. Engineering Manufacture*, 2002, **216**(B9), 1253–1264.
- 12 **Carslaw, H. S. and Jaeger, J. C.** *Conduction of Heat in Solids*, 1959 (Clarendon Press, Oxford).
- 13 **Vinokurov, V. A.** *Welding Stresses and Distortion*, 1987 (Boston Spa, London).
- 14 **Frewin, M. R. and Scott, D. A.** Finite element model of pulsed laser welding. *Weld. J.*, 1999, **78**, 15–22.
- 15 **Siegman, A. E.** *Lasers*, 1986 (University Science Books, Mill Valley, California).
- 16 **Brown, S. and Song, H.** Finite element simulation of welding of large structures. *Trans. ASME, J. Engng for Industry*, 1992, **114**(4), 441–451.
- 17 **DeWitt, D. P. and Nutter, G. D.** *Theory and Practice of Radiation Thermometry*, 1988 (John Wiley, New York).
- 18 **Green, S.** Radiation. Thermometry: an introduction to theory, technology and techniques. *Measure and Control*, 1995, **28**, 238–243.
- 19 **Hu, D., Labudovic, M. and Kovacevic, R.** On-line sensing and estimation of laser surface modification process by computer vision. *Proc. Instn Mech. Engrs, Part B: J. Engineering Manufacture*, 2001, **215**(B8), 1081–1090.